

In-memory factorization of holographic perceptual representations

Jovin Langenegger,^{1,2} Geethan Karunaratne,^{1,2} Michael Hersche,^{1,2} Luca Benini,² Abu Sebastian,^{1, a)} and Abbas Rahimi^{1, b)}

¹⁾IBM Research – Zurich, Säumerstrasse 4, 8803 Rüschlikon, Switzerland.

²⁾Department of Information Technology and Electrical Engineering, ETH Zürich, Gloriastrasse 35, 8092 Zürich, Switzerland.

(Dated: 10 November 2022)

Disentanglement of constituent factors of a sensory signal is central to perception and cognition and hence is a critical task for future artificial intelligence systems. In this paper, we present a compute engine capable of efficiently factorizing holographic perceptual representations by exploiting the computation-in-superposition capability of brain-inspired hyperdimensional computing and the intrinsic stochasticity associated with analog in-memory computing based on nanoscale memristive devices. Such an iterative in-memory factorizer is shown to solve at least five orders of magnitude larger problems that cannot be solved otherwise, while also significantly lowering the computational time and space complexity. We present a large-scale experimental demonstration of the factorizer by employing two in-memory compute chips based on phase-change memristive devices. The dominant matrix-vector multiply operations are executed at $\mathcal{O}(1)$ thus reducing the computational time complexity to merely the number of iterations. Moreover, we experimentally demonstrate the ability to factorize visual perceptual representations reliably and efficiently.

INTRODUCTION

One of the fundamental problems in perception is unbinding—the separation of causes of a raw sensory signal¹ that contain multiple attributes. For instance, the pixel intensities sensed by photoreceptors result from the combination of different physical attribute factors^{1–5}. In fact, the observed luminance at a point on the sensor is a multiplicative combination of reflectance and shading factors². To be able to infer these factors, visual perception must begin with the observed luminance and solve an inverse problem that involves undoing the multiplication by which the factors were combined^{1,3}. This factorization problem is also at the core of other levels of the conceptual hierarchy, such as factoring time-varying pixel data of dynamic scenes into persistent and dynamic factors^{6–9}, factoring a sentence structure into roles and fillers^{10,11}, and finally cognitive analogical reasoning^{12–16}. How these factorization problems could be solved efficiently by biological neural circuits is still unclear to date. Moreover, given their ubiquitous presence in perception and cognition, it is essential that future artificial intelligence systems are equipped with compute units that can perform these factorization operations efficiently across very large problem sizes.

We propose a non-deterministic non-von Neumann compute engine that efficiently factorizes holographic representations combining the emerging compute paradigm of in-memory computing (IMC)^{17–19} with a resonator network^{20,21}. The resonator network, a viable neural solution to the aforementioned factorization problems, is a nonlinear dynamical system capable of factorizing high-dimensional holographic vectors based on properties of brain-inspired vector symbolic architectures^{22–25} (see Supplementary Note 1). An object with F attribute factors can be described by element-wise multiplication of its associated D -dimensional holographic bipolar ($\{-1, +1\}^D$) vectors which results in a unique product vector of the same fixed dimensionality²⁰. Now, given a raw image of an object, a deep convolutional neural network can be trained to generate the product vector approximately²⁸ which in turn can be factorized by the resonator network. It searches for the F factors across a set of possible solutions, called codevectors, that are associated with each factor. Per factor, the union of all associated codevectors is called a codebook (see Fig. 1a, with $F = 3$). All codevectors are randomly drawn which makes them quasi-orthogonal to each other in the high-dimensional space. When each codebook contains a finite set of M codevectors, there are M^F possible combinations to be searched in order to factorize the D -dimensional product vector into its constituent factors, where $D \ll M^F$. Factorizing the product vectors constructed by binding randomly drawn vectors that exhibit no correlational structure forms a hard combinatorial search problem. By exploiting the quasi-orthogonality of codevectors, the resonator network is able to rapidly search these many combinations in superposition by iteratively multiplying (i.e., unbinding) all but one of the factors with the product vector, and then projecting it into the space of possible solutions of the considered factor. Both the similarity search and projection operations associated with the resonator network involve matrix-vector multiply (MVM) operations where the matrix transpires to be a fixed codebook. This is highly amenable to IMC using memristive devices^{26,27}. Moreover, the intrinsic stochasticity of the devices could be a valuable computational tool as has been proposed for solving combinatorial optimization problems such as annealing²⁹, Boltzmann machines^{30–33}, and Hopfield networks^{34–36}.

^{a)}Electronic mail: ase@zurich.ibm.com

^{b)}Electronic mail: abr@zurich.ibm.com

The proposed in-memory factorizer stores the codevectors on crossbar arrays of memristive devices performing analog in-memory MVM operations. As shown in Fig. 1b, the similarity calculation and projection are based on MVM and transposed MVM operations, respectively. These operations can be executed in-memory in a crossbar array of memristive devices by exploiting the Ohm's law and Kirchhoff's current summations law. Moreover, the intrinsic stochasticity associated with the memristive devices can be exploited to enhance the maximally solvable problem size. Finally, we present a large-scale experimental demonstration using in-memory compute cores based on phase-change memory (PCM) technology and applications in visual perception.

I. IN-MEMORY STOCHASTIC FACTORIZER WITH SPARSE ACTIVATIONS

The unsupervised nature of the resonator network's deterministic search procedure could result in checking the same sequence of solutions multiple times across iterations, resulting in limit cycles that prevent convergence to the optimal solution. One of the key insights from the in-memory factorizer is that the intrinsic stochasticity associated with the memristive devices can significantly reduce the occurrence of such limit cycles. As shown in Fig. 2a, during the similarity calculation, the analog in-memory MVM results in a stochastic similarity vector. The stochasticity enables the factorizer to break free of limit-cycles and thus explore a substantially larger solution space (Fig. 2b). Moreover, we find that adopting a winners-take-all approach, by zeroing out the weaker similarity values, enhances the convergence rate of the in-memory factorizer (see Supplementary Note 2). The winners-take-all approach uses an activation threshold, T , to sparsify the similarity vector (Fig. 2a) which was chosen based on Bayesian optimization (see Methods).

The resulting non-deterministic, sparse in-memory factorizer can be analyzed and compared with the state-of-the-art using three figures of merit: the dimensionality, the computational complexity, and the operational capacity. The dimensionality refers to the number of elements in a codevector. The computational complexity defines the average number of the operations required by a factorizer to factorize a given product vector where each operation refers to a D -dimensional dot product calculation. It depends on the problem size and the number of the factors. Given an upper bound for the first two figures of merit, the operational capacity defines the maximally solvable problem size with an accuracy of at least 99%. To compare the operational capacity of the in-memory factorizer with the baseline resonator network^{20,21} we performed extensive simulations of the in-memory factorizer in software (see Methods). As seen in Fig. 3, the in-memory factorizer significantly enhances the operational capacity by up to five orders of magnitude even when the vector dimensionality is reduced by a factor of over four. (Fig. S1).

II. LARGE-SCALE EXPERIMENTAL DEMONSTRATION

Next, we present an experimental realization of the in-memory factorizer using IMC cores based on PCM devices fabricated in 14 nm CMOS technology (see Methods). We employed two IMC cores, one to calculate the similarities and one for the projections (Fig. 4a). Each IMC core features a crossbar array of 256×256 unit-cells capable of performing stochastic and analog MVM operations³⁷. Each unit-cell comprises four PCM devices organized in a differential configuration and can be programmed to a certain conductance value. However, due to the intrinsic stochasticity associated with crystal nucleation and growth, there will be a distribution of conduction values across multiple devices in the crossbar (Fig. 4b). In addition to this, there is read noise that exhibits a $1/f$ spectral characteristic and random telegraph noise. The input to the IMC core is applied using a constant pulse-width modulated voltage applied to all the rows of the crossbar array in parallel. Ohm's law defines the current flowing through each unit-cell and the current is summed up on the corresponding bitlines in accordance with Kirchhoff's current summation law. This current is digitized and accumulated by 256 analog-to-digital converters operating in parallel.

Each IMC core performs MVM operations in $\mathcal{O}(1)$, which leads to reducing the time complexity of factorization to merely the average number of iterations. Moreover, the intrinsic randomness associated with the PCM devices is exploited to calculate the stochastic similarity and projection vectors that minimizes the occurrence of the limit cycles (Fig. 4b and c). A permute logic is employed to temporally multiplex one crossbar array for multiple factors and the hyperparameters such as the activation and convergence thresholds were obtained through Bayesian learning (see Methods). The experimentally realized in-memory factorizer is compared to the baseline resonator network^{20,21}, whereby both methods used $D = 256$, $M = 256$, and $F = 3$. These parameters set the total problem size to $M^F = 16,777,216$, and the maximum number of iterations to $N = 21,845$, which ensures that the computational complexity does not exceed that of the brute-force search (see Methods). When using the same codebooks and 5,000 randomly selected product vectors as queries, the baseline resonator network is found to be incapable of factorizing any of the product vectors. In contrast, the in-memory factorizer is capable of achieving an outstanding accuracy of 99.71% with an average number of 3,312 iterations.

Finally, we demonstrate the role of the in-memory factorizer in visual perception to disentangle the constituents of raw images. The perception system consists of two main components, as shown in Fig. 4d. A convolutional neural network is trained to map the input image to a holographic perceptual product vector, based on a known set of image attribute descriptions. Hence, during inference, the output of the neural network is an approximation of the product vector that describes the image. The in-memory

factorizer is used to disentangle the approximate product vector using a known set of image attributes. For experiments, we used the input images from the relational and analogical visual reasoning (RAVEN) dataset³⁸. The images contain objects with attributes such as type, size, color, and position. Each set of attributes is mapped to a unique codebook leveraging its symbolic nature (see Methods). The disentanglement of 1,000 images from the RAVEN dataset to the desired attributes achieved an accuracy of 99.42% (see Supplementary Video 1).

III. DISCUSSION

We compare the in-memory factorizer with a dedicated reference digital design that benefits from the proposed sparse activations and all other features, except the intrinsic stochasticity that is inherent to the PCM devices. Using the same configurations of the experiments ($D = 256$, $M = 256$, $F = 3$, and 5,000 trials), the deterministic digital design was able to reach an accuracy of 95.76% with 3,802 iterations on average. Compared to the in-memory factorizer, the digital design demanded 14.8% more iterations on average, and still exhibited 4% lower accuracy. Even if we allow the maximum number of iterations to be arbitrarily large, the digital design is still not able to match the accuracy of the in-memory factorizer due to the limit cycles (see Supplementary Note 3) thus highlighting the crucial role of the intrinsic stochasticity associated with the PCM devices.

The in-memory factorizer could also result in significant gain in energy and areal efficiency. By combining the advantages of in-place computation and reduced number of iterations, it is estimated that an in-memory factorizer based on a 512×512 crossbar array is capable of factorizing a single query within an energy budget of $29 \mu\text{J}$ on average, resulting in energy savings of $13.9 \times$ compared to the reference digital design. The total area saving is estimated to be $4.85 \times$ (see Supplementary Note 3). The non-volatile storage of the codebooks is an added advantage compared to the digital design.

Note that the application of in-memory factorizers can go beyond visual perception, as factorization problems arise everywhere in perception and cognition, for instance in analogical reasoning^{12–16,39}. Other applications include tree search²⁰ and prime factorization of integers⁴⁰. Recently, it has been shown how the classical integer factorization problem can be solved by casting it as a problem of factorizing high-dimensional holographic vectors⁴⁰. These pave the way for solving non-trivial combinatorial search problems.

To summarize, we have presented a non-von Neumann compute engine to factorize holographic representations by searching in superposition. We have experimentally verified it using two state-of-the-art in-memory compute cores based on PCM technology. The experimental results show the reliable and efficient factorization of holographic vectors spanning a search space of $256 \times 256 \times 256$. Besides in-place computation and non-volatility, the intrinsic stochasticity associated with the PCM devices is exploited to enhance the operational capacity by five orders of magnitude as well as to reduce the spatial and time complexity associated with the computational task. Furthermore, we demonstrated the efficacy of the in-memory factorizer in disentangling the constituents of raw images. This work also highlights the role of emerging non-von Neumann compute paradigms in realizing critical building blocks of future artificial intelligence systems.

REFERENCES

- ¹Feldman, J. The neural binding problem(s). *Cognitive Neurodynamics*. **7**, 1-11 (2013,2)
- ²Barrow, H. & Tenenbaum, J. Recovering intrinsic scene characteristics from images. *Computer Vision Systems*. pp. 3-26 (1978)
- ³Adelson, E. & Pentland, A. The perception of shading and reflectance. *Perception As Bayesian Inference*. pp. 409-424 (1996)
- ⁴Barron, J. & Malik, J. Shape, Illumination, and Reflectance from Shading. *IEEE Transactions On Pattern Analysis And Machine Intelligence*. **37**, 1670-1687 (2015)
- ⁵Land, E. & McCann, J. Lightness and Retinex Theory. *Journal Of The Optical Society Of America*. **61**, 1-11 (1971,1)
- ⁶Memisevic, R. & Hinton, G. Learning to Represent Spatial Transformations with Factored Higher-Order Boltzmann Machines. *Neural Computation*. **22**, 1473-1492 (2010,6)
- ⁷Cadieu, C. & Olshausen, B. Learning Intermediate-Level Representations of Form and Motion from Natural Movies. *Neural Computation*. **24**, 827-866 (2012,4)
- ⁸Anderson, A., Ratnam, K., Roorda, A. & Olshausen, B. High-acuity vision from retinal image motion. *Journal Of Vision*. **20**, 34-34 (2020,7)
- ⁹Burak, Y., Rokni, U., Meister, M. & Haim Sompolinsky Bayesian model of dynamic image stabilization in the visual system. *Proceedings Of The National Academy Of Sciences*. **107**, 19525-19530 (2010)
- ¹⁰Smolensky, P. Tensor Product Variable Binding and the Representation of Symbolic Structures in Connectionist Systems. *Artificial Intelligence*. **46** pp. 159-216 (1990)
- ¹¹Jackendoff, R. Foundations of Language: Brain, Meaning, Grammar, Evolution. (Oxford University Press,2002)
- ¹²Hummel, J. & Holyoak, K. Distributed Representations of Structure: A Theory of Analogical Access and Mapping. *Psychological Review*. **104**, 427-466 (1997)
- ¹³Kanerva, P. Dual Role of Analogy in the Design of a Cognitive Computer. *Advances In Analogy Research: Integration Of Theory And Data From The Cognitive, Computational, And Neural Sciences*. pp. 164-170 (1998)
- ¹⁴Kanerva, P. Pattern Completion with Distributed Representation. *International Joint Conference On Neural Networks*. pp. 1416-1421 (1998)
- ¹⁵Plate, T. Analogy Retrieval and Processing with Distributed Vector Representations. *Expert Systems: The International Journal Of Knowledge Engineering And Neural Networks*. **17**, 29-40 (2000)
- ¹⁶Gayler, R. & Levy, S. A Distributed Basis for Analogical Mapping: New frontiers in Analogy Research. *New Frontiers In Analogy Research, Second International Conference On The Analogy*. pp. 165-174 (2009)
- ¹⁷Lanza, M., Sebastian, A., Lu, W., Gallo, M., Chang, M., Akinwande, D., Puglisi, F., Alshareef, H., Liu, M. & Juan B. Roldan Memristive technologies for data storage, computation, encryption, and radio-frequency communication. *Science*. **376** (2022)
- ¹⁸Sebastian, A., Le Gallo, M., Khaddam-Aljameh, R. & Eleftheriou, E. Memory devices and applications for in-memory computing. *Nature Nanotechnology*. **15** pp. 529-544 (2020)
- ¹⁹Wang, Z., Wu, H., Burr, G., Hwang, C., Wang, K., Xia, Q. & Yang, J. Resistive switching materials for information processing. *Nature Reviews Materials*. **5**, 173-195 (2020,3)
- ²⁰Frady, E., Kent, S., Olshausen, B. & Sommer, F. Resonator Networks, 1: An Efficient Solution for Factoring High-Dimensional, Distributed Representations of Data Structures. *Neural Computation*. **32**, 2311-2331 (2020)
- ²¹Kent, S., Frady, E., Sommer, F. & Olshausen, B. Resonator Networks, 2: Factorization Performance and Capacity Compared to Optimization-Based Methods. *Neural Computation*. **32**, 2332-2388 (2020)
- ²²Gayler, R. Vector Symbolic Architectures Answer Jackendoff's Challenges for Cognitive Neuroscience. *Joint International Conference On Cognitive Science*. pp. 133-138 (2003)
- ²³Kanerva, P. Hyperdimensional Computing: An Introduction to Computing in Distributed Representation with High-Dimensional Random Vectors. *Cognitive Computation*. **1**, 139-159 (2009)
- ²⁴Plate, T. Holographic Reduced Representations: Distributed Representation for Cognitive Structures. (Stanford University,2003)
- ²⁵Plate, T. Holographic Reduced Representations. *IEEE Transactions On Neural Networks*. **6**, 623-641 (1995)
- ²⁶Wong, H. & Salahuddin, S. Memory leads the way to better computing. *Nature Nanotechnology*. **10**, 191-194 (2015,3)
- ²⁷Chua, L. Resistance switching memories are memristors. *Applied Physics A*. **102**, 765-783 (2011,3)
- ²⁸Hersche, M., Zeqiri, M., Benini, L., Sebastian, A. & Rahimi, A. A Neuro-vector-symbolic Architecture for Solving Raven's Progressive Matrices. *arXiv:2203.04571*. (2022)
- ²⁹Shin, J., Jeong, Y., Zidan, M., Wang, Q. & Lu, W. Hardware Acceleration of Simulated Annealing of Spin Glass by RRAM Crossbar Array. *IEEE International Electron Devices Meeting*. (2018)
- ³⁰Bojnordi, M. & Ipek, E. Memristive Boltzmann machine: A hardware accelerator for combinatorial optimization and deep learning. *IEEE International Symposium On High Performance Computer Architecture*. (2016)
- ³¹Mahmoodi, M., Prezioso, M. & Strukov, D. Versatile stochastic dot product circuits based on nonvolatile memories for high performance neurocomputing and neurooptimization. *Nature Communications*. **10**, 5113 (2019,11)
- ³²Borders, W., Pervaiz, A., Fukami, S., Camsari, K., Ohno, H. & Datta, S. Integer factorization using stochastic magnetic tunnel junctions. *Nature*. **573**, 390-393 (2019,9)
- ³³Wan, W., Kubendran, R., Eryilmaz, S., Zhang, W., Liao, Y., Wu, D., Deiss, S., Gao, B., Raina, P., Joshi, S., Wu, H., Cauwenberghs, G. & Wong, H. 33.1 A 74 TMACS/W CMOS-RRAM Neurosynaptic Core with Dynamically Reconfigurable Dataflow and In-situ Transposable Weights for Probabilistic Graphical Models. *IEEE International Solid-State Circuits Conference*. (2020)
- ³⁴Cai, F., Kumar, S., Van Vaerenbergh, T., Sheng, X., Liu, R., Li, C., Liu, Z., Foltin, M., Yu, S., Xia, Q., Yang, J., Beausoleil, R., Lu, W. & Strachan, J. Power-efficient combinatorial optimization using intrinsic noise in memristor Hopfield neural networks. *Nature Electronics*. **3**, 409-418 (2020,7)
- ³⁵Yang, K., Duan, Q., Wang, Y., Zhang, T., Yang, Y. & Ru Huang Transiently chaotic simulated annealing based on intrinsic nonlinearity of memristors for efficient solution of optimization problems. *Science Advances*. **6** (2020)
- ³⁶Kumar, S., Strachan, J. & Williams, R. Chaotic dynamics in nanoscale NbO₂ Mott memristors for analogue computing. *Nature*. **548**, 318-321 (2017,8)
- ³⁷Khaddam-Aljameh, R., Stanisavljevic, M., Mas, J., Karunaratne, G., Braendli, M., Liu, F., Singh, A., Müller, S., Egger, U., Petropoulos, A., Antonakopoulos, T., Brew, K., Choi, S., Ok, I., Lie, F., Saulnier, N., Chan, V., Ahsan, I., Narayanan, V., Nandakumar, S., Gallo, M., Francese, P., Sebastian, A. & Eleftheriou, E. HERMES Core – A 14nm CMOS and PCM-based In-Memory Compute Core using an array of 300 ps/LSB Linearized CCO-based ADCs and local digital processing. *Symposium On VLSI Technology*. pp. 1-2 (2021)
- ³⁸Zhang, C., Gao, F., Jia, B., Zhu, Y. & Zhu, S. RAVEN: A Dataset for Relational and Analogical Visual rEasoNing. *Proceedings Of The IEEE Conference On Computer Vision And Pattern Recognition*. (2019)

³⁹Kent, S. Multiplicative coding and factorization in vector symbolic models of cognition. (University of California, Berkeley,2020)

⁴⁰Kleyko, D., Bybee, C., Kymn, C., Olshausen, B., Khosrowshahi, A., Nikonov, D., Sommer, F. & Frady, E. Integer Factorization with Compositional Distributed Representations. *The 9th Annual Neuro-Inspired Computational Elements Workshop*. (2022)

⁴¹Kleyko, D., Rachkovskij, D., Osipov, E. & Rahimi, A. A Survey on Hyperdimensional Computing Aka Vector Symbolic Architectures, Part I: Models and Data Transformations. *ACM Comput. Surv.*. (2022,5)

⁴²Kleyko, D., Rachkovskij, D., Osipov, E. & Rahimi, A. A Survey on Hyperdimensional Computing Aka Vector Symbolic Architectures, Part II: Applications, Cognitive Models, and Challenges. *ACM Comput. Surv.*. (2022,6)

⁴³Millidge, B., Salvatori, T., Song, Y., Lukasiewicz, T. & Bogacz, R. Universal Hopfield Networks: A General Framework for Single-Shot Associative Memory Models. *Proceedings Of The 39th International Conference On Machine Learning*. (2022)

⁴⁴Nandakumar, S., Le Gallo, M., Piveteau, C., Joshi, V., Mariani, G., Boybat, I., Karunaratne, G., Khaddam-Aljameh, R., Egger, U., Petropoulos, A., Antonakopoulos, T., Rajendran, B., Sebastian, A. & Eleftheriou, E. Mixed-Precision Deep Learning Based on Computational Memory. *Frontiers In Neuroscience*. **14** pp. 406 (2020)

ACKNOWLEDGEMENTS

This work is supported by the IBM Research AI Hardware Center. We also acknowledge financial support from the Swiss National Science Foundation. The authors would also like to thank M. Le Gallo for technical support.

DATA AVAILABILITY

All data needed to evaluate the conclusions in the paper are present in the paper or the supplementary information.

CODE AVAILABILITY

The code used to generate the results of this study are available from the corresponding authors upon request.

AUTHOR CONTRIBUTIONS

J.L., G.K., M.H., A.S., and A.R. conceived the idea and designed the experiments. J.L. performed experiments and characterization. J.L., A.S., and A.R. wrote the manuscript with input from all authors. All authors provided critical comments and analyses.

COMPETING INTERESTS

The authors declare no competing interests.

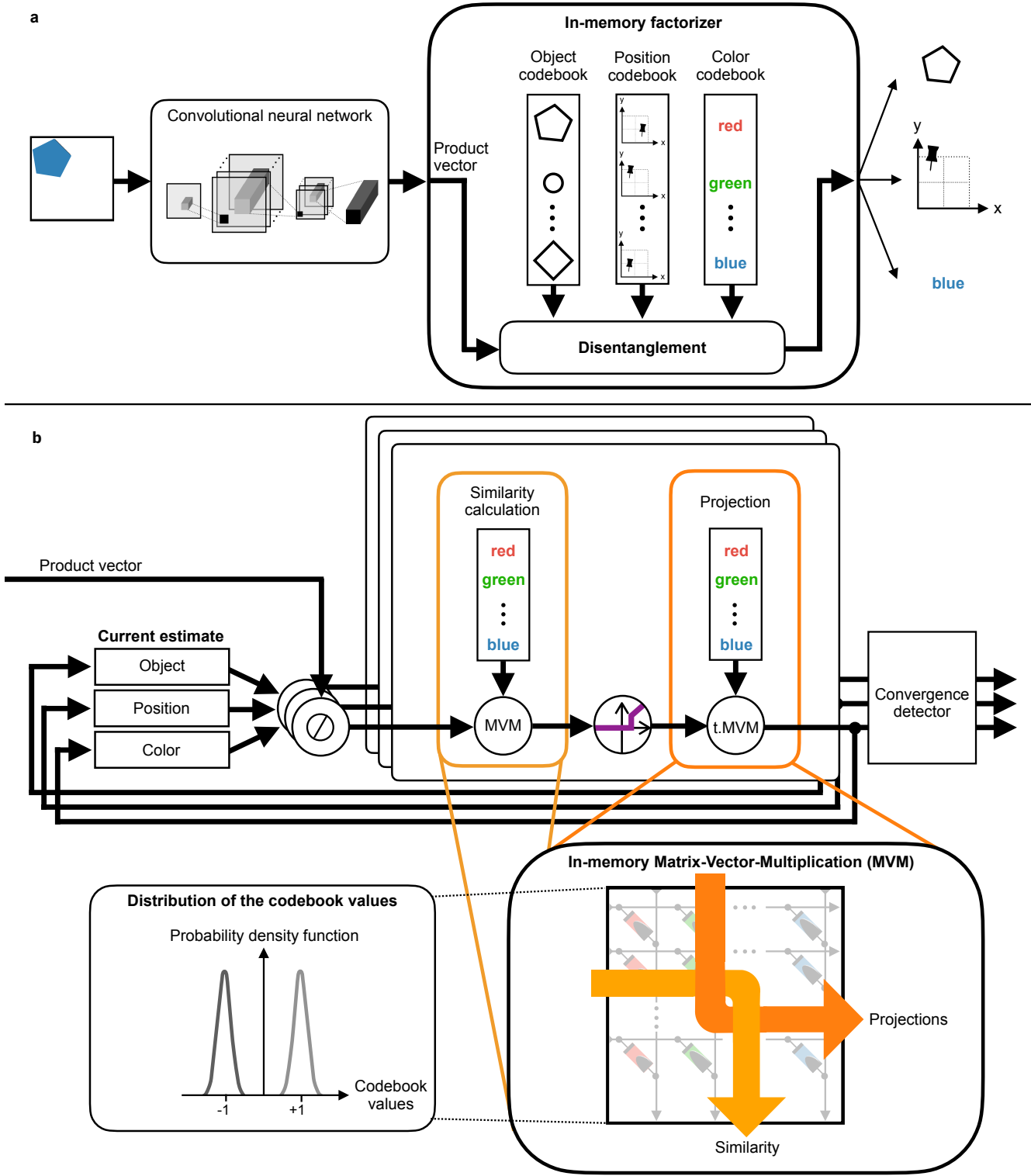


Fig. 1 | Factorization of perceptual representations using the in-memory factorizer. (a) The visual input is first fed through a convolutional neural network to approximately map it to a D -dimensional product vector. The generated product vector is applied as an input to the in-memory factorizer, which contains a unique codevector for each possible attribute value in an associated codebook. The factorizer disentangles the product vector and predicts the underlying factors out of all possible combinations of the attributes. (b) The in-memory factorizer iteratively searches in superposition. For each attribute an updated estimate is computed during every iteration by unbinding the contribution of the other factors from the product vector. The unbound estimate is fed through the similarity calculation and the projection to obtain a novel estimate, which is then fed back to be used in the next iteration. Similarity calculation is based on MVM operations, and projection is based on transposed MVM operations that can both be executed in-memory in a crossbar array of memristive devices by exploiting the Ohm's law and Kirchhoff's current summations law with a computational time complexity of $\mathcal{O}(1)$. Moreover, the intrinsic stochasticity associated with storing the bipolar codevectors in the array and the resulting imprecise MVM operations serve as a key enabler for the in-memory factorizer.

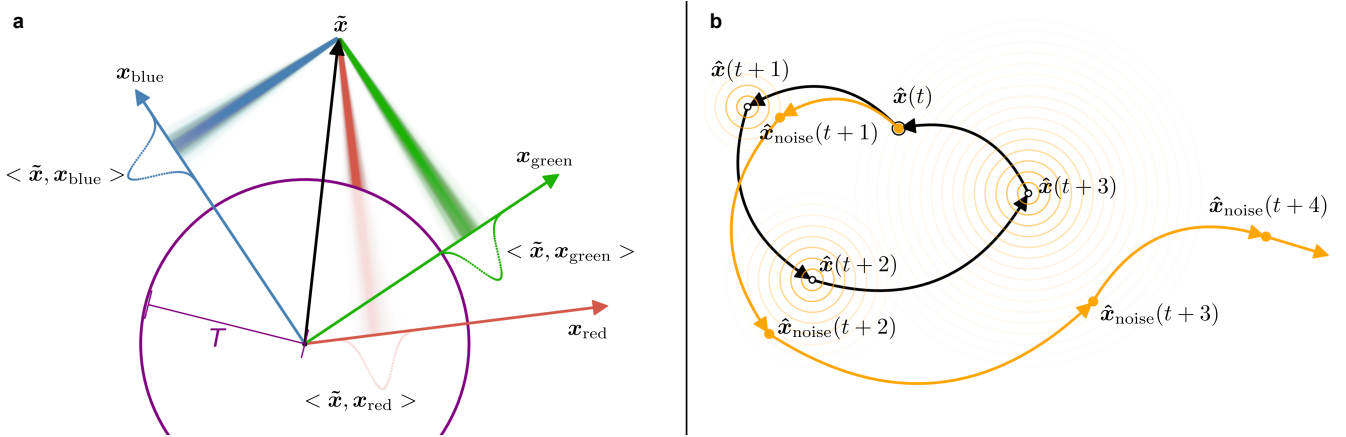


Fig. 2 | Stochastic similarity computation, sparse activations, and limit cycles. (a) The similarity calculation computes the similarities between the unbound estimate vector \tilde{x} and all the codevectors (e.g., $\{x_{red}, x_{green}, x_{blue}\}$). The in-memory similarity calculation, denoted by $\langle \cdot, \cdot \rangle$, is stochastic with an additive noise. The distribution of noisy similarity results projected onto the 2-D space is shown in green, red, and blue colors respectively. Further, a winners-take-all approach *activates* similarity values only above a certain threshold (T) level which results in a similarity vector with sparse non-zero elements. Similarity values smaller than T are zeroed out, for instance $\langle \tilde{x}, x_{red} \rangle$ is not activated (i.e., zeroed), while the other two similarity values ($\langle \tilde{x}, x_{blue} \rangle$ and $\langle \tilde{x}, x_{green} \rangle$), larger than T , remain activated. The activation threshold (T) is depicted in purple. (b) Visualized by the black arrows, this figure shows a limit cycle of length $l=4$. When stuck in a limit cycle of length l , we end up constantly checking the same l solutions. In contrast, the orange arrows show an example trajectory of the factor's estimates (\hat{x}) of the in-memory factorizer exploiting stochasticity in both similarity and projection operations which yields noisy estimates. For a subsequent time step, there is some uncertainty as visualized by the orange circles. As the search for factorization is an iterative process, the uncertainty for the subsequent time steps increases. Eventually the uncertainty is high enough for the in-memory factorizer to diverge from a limit cycle, and to converge to the correct factorization in time.

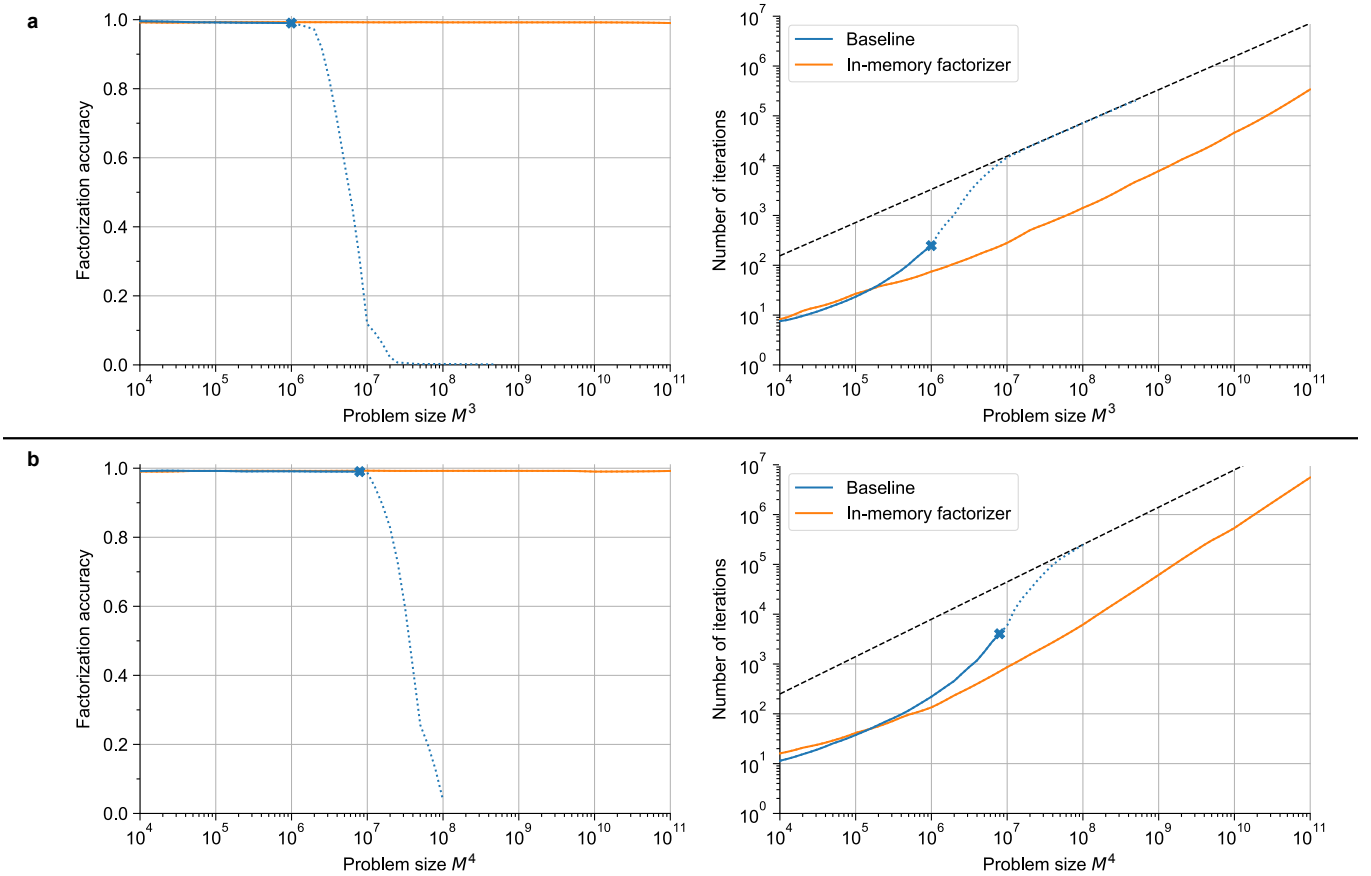


Fig. 3 | Operational capacity of the stochastic in-memory factorizer with sparse activations. This figure shows the operational capacity for: $F=3$ in (a), and $F=4$ in (b). The problem size M^F is shown on the X-axis, and the Y-axis shows the accuracy on the left side of the plot, and the number of iterations required to solve a given problem size on the right side. The black dashed lines indicate the equivalent number of dot-product operations required for a brute-force approach to search among M^F precomputed product vectors. These lines indicate the upper limit for the operation count. For each F , we use the smallest dimension reported by the baseline resonator network^{20,21}, namely $D=1500$ for $F=3$, and $D=2000$ for $F=4$. The blue cross indicates the largest problem size that is within the operational capacity of the baseline resonator network, meaning that the problems larger than that size can not be factorized by the baseline network at 99% accuracy, while the in-memory factorizer can solve at least five orders of magnitude larger problem sizes at 99% accuracy, or higher.

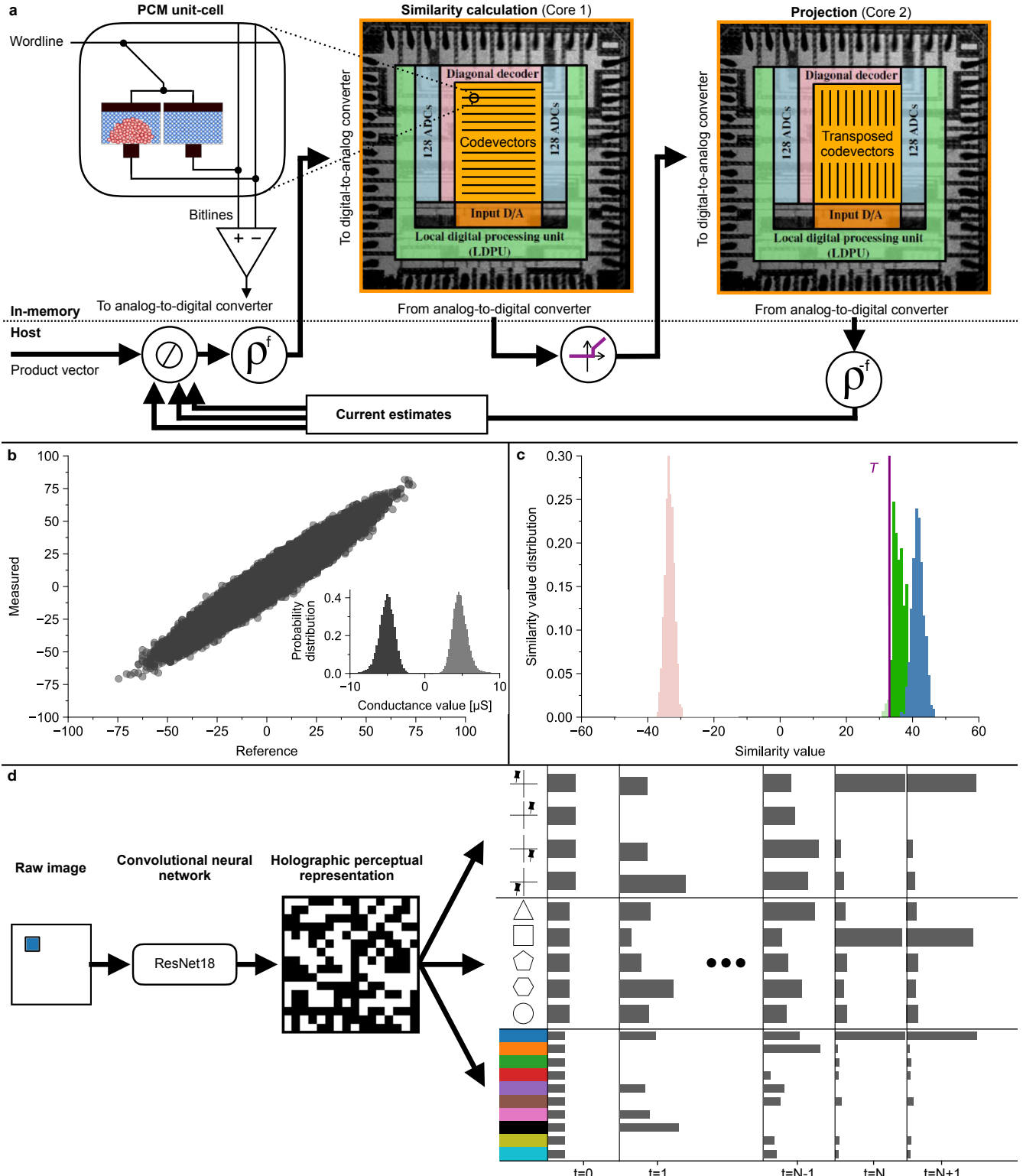


Fig. 4 | Experimental realization of the in-memory factorizer. (a) Our experimental setup includes two IMC cores for similarity calculation and projection. Each MVM operation is executed using the crossbars and the fully integrated peripherals on one of the two cores. The unbinding, permutation, activation, and bipolarization operations are executed on the host computer connected to the setup. On the crossbar, one unit cell stores one bipolar (± 1) weight value associated with the codevectors. In the first core, the codevectors are stored along the columns of the crossbar, while in the second core, the codevectors are stored along the rows. Each unit-cell is programmed to the desired value. (b) The measured output of the in-memory MVM plotted against the reference output obtained in high precision indicating the intrinsic stochasticity associated with the operation. The inner panel shows the distribution of the programmed conductance values on the first core executing the similarity calculation. The gray histogram corresponds to the positive conductance values, and the black histogram to the negative ones. The target conductance value was set at $5\mu\text{S}$. (c) The red, green, and blue histograms correspond to the distribution of similarity between the same unbound estimate vector (\hat{x}) and three color codevectors of x_{red} , x_{green} , x_{blue} , respectively. The purple vertical line corresponds to the activation threshold at $T=33$, which avoids activating any similarity values related to x_{red} . (d) The raw image is fed through a ResNet18 to generate the holographic perceptual representation visualized as a binary heatmap. The in-memory factorizer iteratively disentangles the holographic representation. At the first time step, all codevectors show an equal similarity to the current estimate. Over time, the in-memory factorizer converges to the correct factorization, indicated by a high similarity value for a single codevector.

METHODS

Detection of convergence in the in-memory factorizer

The iterative factorization problem is said to be converged if, for two consecutive time steps, all the estimates are constant, i.e., $\hat{x}^f(t+1) = \hat{x}^f(t)$ for $f \in [1, F]$. To detect this convergence, we define a novel early convergence detection algorithm. The in-memory factorizer is said to be converged if a single similarity value across all the factors surpasses a convergence detection threshold:

$$\text{converged} = \begin{cases} \text{true,} & \text{if } \alpha_i^f > T_{\text{convergence}} \\ \text{false,} & \text{otherwise,} \end{cases} \quad (1)$$

where $i \in [1, |X^f|]$ for $f \in [1, F]$. Upon convergence, the predicted factorization is given by the codevector associated with the largest similarity value per codebook. The novel convergence detection counteracts parasitic codevectors with a high enough similarity value to prevent the in-memory factorizer from converging to a stable solution. Further, there is no need to store historic estimate data at all.

Otherwise, the last estimate for each factor had to be stored to be able to compare it to the latest estimate and detect convergence, resulting in a total of $F \cdot D$ stored bits. We used Bayesian optimization to find the optimal convergence detection threshold. It stays at a fixed ratio of D for any given set of hyperparameters and problem sizes.

Maximal number of iterations

To use strictly less search operations compared to the brute-force approach, the maximal number of iterations (N) must be constrained to:

$$N \cdot M \cdot F < M^F. \quad (2)$$

In all our experiments, we constrain the maximum number of iterations to $N < \frac{M^{F-1}}{F}$ to ensure a lower computational complexity compared to the brute-force approach.

Hyperparameter optimization via Bayesian optimization

We find the optimal hyperparameters of the in-memory factorizer $\mathbf{h}^* = [T^*, T_{\text{convergence}}^*]$ by solving a Bayesian optimization problem where T^* is the activation threshold and $T_{\text{convergence}}^*$ is the convergence threshold. We define the error rate l to be the ratio of the wrongly factorized product vector. More formally, we try to find the optimal set of hyperparameters \mathbf{h}^* by minimizing the error rate l , which is a function of the hyperparameters \mathbf{h} :

$$\mathbf{h}^* = \arg \min_{\mathbf{h}} l(\mathbf{h}). \quad (3)$$

We model the error rate as a Gaussian process with a radial basis function kernel and minimize it using Bayesian optimization. To sample possible hyperparameters during the optimization we use the expected improvement acquisition function.

We reduce the computational complexity of the error rate evaluation for a given set of hyperparameters \mathbf{h} by limiting the maximum number of iterations to $N' = N/10$ and the number of trials to 256. A low number of iterations N' yields higher error rates, yet they still provide a good indications for the in-memory factorizer's performance given a set of hyperparameters. Additionally, the reduced number of trials gives noisy evaluations of l , which is modeled as additive Gaussian measurement noise.

We derived the final parameter estimates by averaging over the best five experiments. For the in-memory factorizer hardware experiments, the stochasticity is inherently provided by the PCM crossbar arrays. However, for simulating our factorizer method in software, we need to model stochasticity as a noise level. Hence, the noise level (n^*) is treated as an extra hyperparameter for optimization. Accordingly, for simulating our method in software we optimized for three hyperparameters: the activation threshold, the convergence threshold, and the noise level, given by $\mathbf{h}^* = [T^*, T_{\text{convergence}}^*, n^*]$.

In-memory experiments

For the experimental demonstration, we employed the HERMES in-memory compute core³⁷. It features 256×256 unit cells each comprising four PCM devices arranged in a differential configuration. A custom printed circuit board houses two such

HERMES cores and an FPGA board is used to control the communication protocol and loading data to and from the cores. The FPGA in turn is controlled by a Linux machine running a Python environment on top.

The host machine performs the unbinding and applies the activation function, while the two cores perform the dominant MVM similarity search and the projection operations, respectively. An iterative programming scheme of the PCM devices is employed to store the codevectors in the crossbars. The output of the in-memory MVM is measured in terms of the ADC count units. Subsequently, a linear correction is applied to correct for circuit-level mismatches. The linear correction's parameters are calculated prior to MVM operations.

The single crossbar core with the dimension of 256×256 limits the total number of the supported codevectors across all the codebooks to 256. To overcome this limitation, we propose a permute logic to temporally multiplex one single crossbar array for all F factors. This enables us to exploit the complete crossbar for one single codebook with up to 256 codevectors, and reuse it across an arbitrary number of factors. As shown in Fig. 4a, prior to the similarity calculation, we apply the permute logic as a factor-wise exclusive circular shift on the estimated unbinding. This results in a quasi-orthogonal time multiplexing of the crossbar. Before updating the estimates, we reverse the circular shift to obtain unaltered estimates.

Software simulations of the in-memory factorizer

The stochasticity is the key enabler of the in-memory factorizer. Adding some stochasticity helps to diverge from the limit cycles as each solution becomes unique. For the experiments reported in Fig. 3, this important aspect is modeled in software by simulating the noisy behaviour of the MVMs on the crossbar as an additive Gaussian noise with zero mean:

$$\alpha'_i = f(\alpha_i) = \alpha_i + n, \quad (4)$$

where α_i is a single entry of the output vector, and n is normally distributed with $n \sim \mathcal{N}(0, \sigma^2)$.

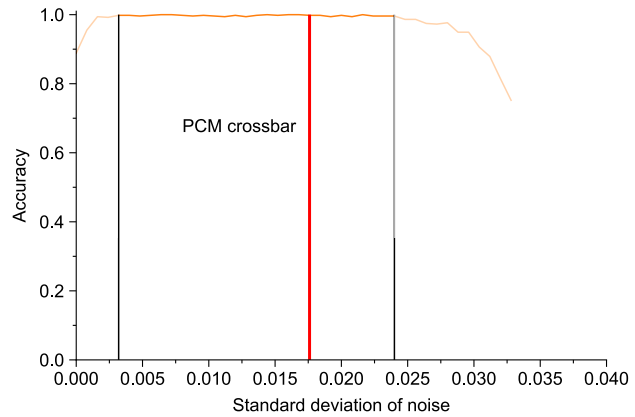
In total, we simulated $F \times (M + D)$ additive Gaussian noise sources: M on the similarity vector and D on the projection vector. The noisy similarity vector is required to break free of the limit cycles. Due to the random distribution of the similarity values, there is always a chance of activating no similarity value if not one reaches the activation threshold. Adding noise on top of the projection prevents such all zero estimation by randomly initializing the vector prior to the bipolarization. The standard deviation of the noise matters for the factorization performance. Below the lower bound of the desirable level of the noise, the factorizer fails to avoid limit cycles. The stochasticity is not sufficient to guide the factorizer's search path clear of limit cycles. Similarly, increasing the noise beyond the upper bound results in a purely random search path. The normalized optimal noise level's standard deviation lies within [0.0032, 0.0240], as shown in Extended Data Fig. 1. The measured standard deviation of the crossbar's noise is at 0.01832, and therefore well within the desirable range of the noise.

Visual disentanglement

We use the RAVEN³⁸ dataset, which provides a rich set of Raven's progressive matrices tests, for visual abstract reasoning tasks. We only focus on the visual perception part of the task to disentangle an image sensory input from its underlying attribute factors. The RAVEN dataset provides a total of 70,000 tests, each consisting of 16 panels of images. In our experiment, we considered the 2x2 image constellation with a single object. Each object can have one of 4 possible positions, 10 colors, 6 sizes, and 5 types. Therefore, there are 1200 possible combinations. We mapped each set of attributes to a single codebook of the in-memory factorizer. Here, we reused the same codebook as for the synthetic experiment. The first codebook represents the position attribute, the second one represents the color attribute. For the third codebook, we fused the size and type attributes into a single codebook, ending up with a total of 30 possible size-type combinations.

Each image can be described as a product vector formed by the binding of the corresponding codevectors. To map the input image to the product vector, we used a convolutional neural network. We used the ResNet-18 convolutional neural network, and mapped its output to our 256-dimensional vector space using the training schema proposed in²⁸. After training, we ran all the test images through the trained ResNet-18 network to get an estimate of the product vector.

Next, we passed all the estimated product vectors through the same experimental test setup used for the the synthetic experiments. The main difference lies in the product vector: while for the synthetic one we used the exact product vectors, for the visual perception task the product vectors are the output of the convolutional neural network, which is an approximate product vector as opposed to the exact one.



Extended Data Fig. 1 | Desirable range of noise. This figure shows the relation between the additive noise level and the accuracy of factorization. The noise is measured in relation to the cosine similarity. The optimal range for the noise lies between 0.32% and 2.40%. Higher noise level show a significant decrease in the accuracy. As indicated by the red vertical line, the noise level of a single MVM on the crossbar lies within the desirable range of the noise.

SUPPLEMENTARY NOTES

Supplementary Note 1: Background in vector symbolic architectures and resonator networks

Vector symbolic architectures

Here, we provide a brief overview of vector symbolic architectures (VSAs)^{22–25} of which the resonator networks^{20,21} are based on. VSA is a powerful computing framework that is built on an algebra in which all representations are high-dimensional holographic vectors of the same, fixed dimensionality denoted by D . In this work, we consider a VSA model based on bipolar vector space²², i.e., $\{-1, +1\}^D$. The similarity between two vectors is defined as the cosine similarity:

$$\text{sim}(\mathbf{x}_1, \mathbf{x}_2) = \frac{\langle \mathbf{x}_1, \mathbf{x}_2 \rangle}{\|\mathbf{x}_1\| \|\mathbf{x}_2\|} = \frac{\langle \mathbf{x}_1, \mathbf{x}_2 \rangle}{D} \quad (\text{S1})$$

As one of the main property of the high-dimensional vector space, any two randomly drawn vectors lie close to quasi-orthogonality to each other, i.e., their expected similarity is close to zero with a high probability²³. The vectors can represent symbols, and can be manipulated by a rich set of dimensionality-preserving algebraic operations:

- Binding: Denoted by \odot , the Hadamard (i.e., element-wise) product of two input vectors implements the binding operation. It is useful to represent hierarchical structure whereby the resulting vector lies quasi-orthogonal to all the input vectors. The binding operation follows the commutative law $\mathbf{x}_1 \odot \mathbf{x}_2 = \mathbf{x}_2 \odot \mathbf{x}_1 = \mathbf{p}$.
- Unbinding: The unbinding operation reverses the binding operation. As the element-wise multiplication in the bipolar space is self-inverse, the same operation as for the binding can be used. Using the unbinding operator \oslash the operation is defined as $\mathbf{p} \oslash \mathbf{x}_1 = \mathbf{x}_2$.
- Bundling: The superposition of two vectors is calculated by the bundling operation \oplus . The operation is defined by an element-wise sum with consecutive bipolarization. In case of an element-wise sum equals to zero, we randomly bipolarize.
- Clean up: The clean-up operation maps a noisy vector to its noise-free representation by an associative memory lookup.
- Permutation: Permutation is a unary operation on a vector that yields a quasi-orthogonal vector of its input. This operation rotates the coordinates of the vector. A simple way to implement this is as a cyclic shift by one position.

Interested readers can refer to a detailed survey^{41,42} about VSAs.

Resonator networks for iterative factorization

Here, we consider a specific form of factorization in which a product vector, based on high-dimensional holographic representations of VSAs, can be factorized into its factors. For each factor, a set of possible solutions is stored in a so-called codebook. Each codebook X contains M possible solutions called codevector of $\{-1, +1\}^D$:

$$X := \{\mathbf{x}_1, \mathbf{x}_2, \dots, \mathbf{x}_M\}. \quad (\text{S2})$$

The number of factors is defined as F . Multiplicative binding among these codebooks forms a total problem size of M^F to be searched (i.e., all possible combinations of codevectors). The codevectors are drawn randomly (hence they are quasi-orthogonal), and are combined by multiplicative binding that is a *randomizing* operation. This creates a combinatorial search for factorization because the resulting M^F quasi-orthogonal vectors in the search space share no particular correlational structure. A brute-force approach requires to search along all possible combinations. In contrast, the resonator networks^{20,21} exploit the VSA operations to iteratively search in superposition for factorizing a given product vector.

Given an entangled (bound) product vector \mathbf{p} and the set of codebooks X^1, X^2, \dots, X^F , the resonator network iteratively searches in superposition to find a valid factorization $\hat{\mathbf{x}}^1 \in X^1, \hat{\mathbf{x}}^2 \in X^2, \dots, \hat{\mathbf{x}}^F \in X^F$ such that the estimated vector $\hat{\mathbf{p}} = \hat{\mathbf{x}}^1 \odot \hat{\mathbf{x}}^2 \odot \dots \odot \hat{\mathbf{x}}^F$ resembles with the highest similarity to the input product vector \mathbf{p} . The initial estimates (at $t = 0$) for the factors $\hat{\mathbf{x}}^1(0), \hat{\mathbf{x}}^2(0), \dots, \hat{\mathbf{x}}^F(0)$ are obtained by superposing all the codebook elements. This provides each element in the codebook an equal chance. At any time step t , the unbound estimates are calculated first. For a given factor, the unbinding is performed by taking the product vector \mathbf{p} and unbinding the contribution of the other factors' latest estimate:

$$\begin{aligned}
\tilde{\mathbf{x}}^1(t) &= \mathbf{p} \oslash \hat{\mathbf{x}}^2(t) \oslash \hat{\mathbf{x}}^3(t) \oslash \cdots \oslash \hat{\mathbf{x}}^F(t) \\
\tilde{\mathbf{x}}^2(t) &= \mathbf{p} \oslash \hat{\mathbf{x}}^1(t) \oslash \hat{\mathbf{x}}^3(t) \oslash \cdots \oslash \hat{\mathbf{x}}^F(t) \\
&\dots \\
\tilde{\mathbf{x}}^F(t) &= \mathbf{p} \oslash \hat{\mathbf{x}}^1(t) \oslash \hat{\mathbf{x}}^2(t) \oslash \cdots \oslash \hat{\mathbf{x}}^{F-1}(t)
\end{aligned} \tag{S3}$$

Secondly, the similarity vector $\boldsymbol{\alpha}^f(t)$ is calculated using a matrix-vector multiplication (MVM). The similarity values are computed for each unbound estimate:

$$\boldsymbol{\alpha}^f(t) = \tilde{\mathbf{x}}^f(t) \cdot \mathbf{X}^f, \forall f \in [1, F] \tag{S4}$$

The estimates for the factors for the subsequent time step are given by the bipolarized, linear combination of all the codevectors with the similarity vectors acting as weights:

$$\hat{\mathbf{x}}^f(t+1) = \text{sign}(\boldsymbol{\alpha}^f(t) \cdot (\mathbf{X}^f)^T), \forall f \in [1, F] \tag{S5}$$

There is an alternative update approach: updating the factor's estimate sequentially. For every time step t , we start with updating the first factor's estimate $\hat{\mathbf{x}}^1(t+1)$ only. To update the second factor $\hat{\mathbf{x}}^2(t+1)$ we use the novel estimate of the first factor $\hat{\mathbf{x}}^1(t+1)$ and the latest estimates $\hat{\mathbf{x}}^f(t), \forall f \in [3, F]$. Equally, the update procedure continues until the last factor is updated always using the latest known estimate for each factor. We chose this sequential updating approach because it yields in a better performance for the resonator network.

The resonator network is said to be stuck in a limit cycle of length l if all the estimated codevector reoccur after l time steps but different codevectors occur in between as defined in equation (S6). In a deterministic implementation of the resonator network, there is no chance of breaking free of limit cycles resulting in non-convergence.

$$\hat{\mathbf{x}}^f(t+l) = \hat{\mathbf{x}}^f(t), \forall f \in [1, F] \tag{S6}$$

Supplementary Note 2: Activation functions

The activation function is applied on the computed similarity values prior to the projection. A proper activation function would aim to *separate* strong similarity values from the weak ones⁴³. In the following, we discuss and elaborate on different types of activation functions.

Identity activation

The neutral activation function is the identity function. There is no differentiation between strong and weak similarity values; the activation functions treats all the similarity equally. The identity function is used in the resonator networks^{20,21} and considered here as a baseline activation function.

Sorting-based activation

One possible implementation to separate the strong similarity values from the weak ones is to keep only the K strongest similarity values. This activation function requires a sorting algorithm globally across all similarity values. Mathematically one can describe the sorting-based activation function as:

$$\alpha'_i = S(\alpha)_i = \begin{cases} \alpha_i, & \text{if } \alpha_i \in \text{top}K(\alpha) \\ 0, & \text{otherwise,} \end{cases} \quad (\text{S7})$$

where K is a tunable hyperparameter. We chose the sorting-based activation to select only the strongest positive values. However, the sorting algorithm is costly for an implementation in hardware.

Threshold-based activation

To separate the strong similarity values from the weak ones, we propose a threshold-based activation function. The proposed activation function applies a threshold T on the similarity vector approximating a sorting-based $\text{top}K$. Following a winners-take-all approach the activation function zeroes out the weak similarity values not reaching the given threshold. Similarity values that surpass the threshold are kept which yields a sparsely activated similarity vector:

$$\alpha'_i = S'(\alpha)_i = \begin{cases} \alpha_i, & \text{if } \alpha_i > T \\ 0, & \text{otherwise.} \end{cases} \quad (\text{S8})$$

This novel activation allows a local (as opposed to global sorting) and hardware-friendly implementation. The threshold is constant across iterations and dimensions.

On average, any given threshold activates a certain number of similarity values denoted by K . To map any desired number of activated values to a threshold T , we aim to find a function $T = f(K, D, M)$. We start by exploiting the randomness property of the high-dimensional vector space in which the similarity values are concentrated around a mean value. The distribution of the similarity values can be approximated by the normal distribution:

$$\Pr(\alpha) = \frac{1}{\sigma\sqrt{2\pi}} e^{-(\alpha-\mu)^2/2\sigma^2}, \quad (\text{S9})$$

where $\mu = 0$ and $\sigma = \frac{1}{\sqrt{D}}$. To statistically activate a given number of K similarity values, we first calculate the ratio between the similarity values to be activated and the total number of the similarity, given by the size of the corresponding codebook M :

$$r = K/M. \quad (\text{S10})$$

To calculate a threshold such that on average only K values exceed it, we invert the given ratio to find the ratio of deactivated similarity values:

$$p = 1 - r = 1 - K/M \quad (\text{S11})$$

Using the quantile function F_T (inverse probability density function) of the normal distribution we calculate a threshold such that on average only K values exceed it. In terms of the distribution function F_T , the quantile function returns the threshold T such that:

$$F_T(t) := \Pr(T \leq t) = p \quad (\text{S12})$$

Using Bayesian optimization we derived K^* , the optimal number of the activated similarity values for each combination of D , F , and M . The optimal number K^* strongly depends on the number of the factors F and weakly on the dimensions D , while it does not depend on the codebook size M . Fig. S2 shows the correlation between the optimal number of the activated values K^* and the corresponding threshold T^* . For a fixed dimension D and number of the factors F , the optimal number of the activated values K^* remains constant for different sizes of the codebook M . This finding simplifies the optimal parameter search, as for a given dimension D and number of the factors F only one single hyperparameters K^* as to be found. Knowing K^* , D and M the optimal threshold can be calculated accordingly to the equations (S8) to (S12) (see Table S1). For both threshold-based and sorting-based activations, we ended up with a comparable optimal number of the activated similarity values. Obviously, the sorting-based activation function is only capable of activating $K \in \mathbb{N}^+$ values, while the threshold-based activation function leads to $K \in \mathbb{R}^+$.

The sorting-based and the threshold-based activation functions perform equally as seen in Fig. S1. Exploiting the threshold-based activation function, the dimensions of the in-memory factorizer can be reduced by at least four times without any decrease of the operational capacity.

Supplementary Note 3: Hardware design

Here, we provide an analysis and comparison of hardware designs dedicated to the energy-efficient execution of the in-memory factorizer. Our proposed analog in-memory hardware design performs the dominant similarity calculation and projection on the next generation in-memory crossbar arrays together with analog peripherals such as input pulse width modulation (PWM) circuits and analog to digital conversion (ADC) circuits. The remaining operations including unbinding, permutations and the activation function are implemented on dedicated peripheral digital CMOS circuits.

We compare the proposed in-memory factorizer's hardware design with a dedicated reference design comprising digital CMOS multipliers and accumulators to perform MVM operations in similarity calculation and projection. To implement the remaining operations in the reference design, the peripheral digital logic modules designed for the in-memory factorizer are reused.

To get a performance estimation of the respective designs, we designed the digital logic modules using *SystemVerilog* and synthesized them with Samsung's 14 nm LPP technology node using Cadence's *Genus* synthesizer tool. The digital circuits are run at a frequency of 10 MHz, yielding a clock period of 100 ns. This allows the peripheral digital circuits to synchronize with the in-memory crossbar arrays which operate with approximately the same delay. For the power estimation, we used the typical corner case which applies a supply voltage of 0.8 V and assumes a temperature of 25°C. All conditions applicable to running the digital circuits are presented in Table S2. The switching activity of the digital netlist is derived via post-synthesis simulation.

To estimate the energy consumed by the analog circuits, we consider the conditions given in Table S2 and apply them to the improved versions of analog crossbar designs discussed in^{37,44}. Analog circuit's energy consists of five parts:

- The energy for PWM generation: This energy is calculated as a function of mean power dissipated by digital circuits that drive the PWM pulses to the source lines, the active time of PWM, and the number of active source lines.
- The energy for charging and discharging source line capacitance: This energy is calculated as a function of source line capacitance, supply voltage, the number of active rows, and columns on the crossbar.
- The energy dissipated on the crossbar: This energy is calculated as a function of read voltage, the number of active rows and columns, average device conductance, supply voltage, and active time of PWM.
- The energy for biasing the regulators at the end of bit lines: This energy is calculated as a function of regulator bias current, supply voltage, maximum PWM active time, and the number of active columns(bit-lines) on the crossbar.
- The energy for analog to digital conversion of the output: This energy is calculated as a function of energy per conversion step and the number of active columns on the crossbar.

The main functional difference between the proposed analog design and the reference digital design is that the reference design's MVM output does not include any stochastic noise sources whereas the proposed in-memory factorizer inherently does. For this reason, for a given dimension D and problem size M , the two designs demonstrate different average accuracy and different average number of iterations. For example, at $D = 256$, $M = 256$, the proposed analog design converges to correct results with 99.74% accuracy using 3058 iterations on average (i.e., within the operational capacity), whereas the reference digital design only achieves 95.76% accuracy using on average 3802 iterations. Hence, this combination of parameters ($D = 256$, $M = 256$) does not lead to the same operational capacity and is not a fair point to compare the two designs.

Instead, we experiment with increasing the dimensionality of the reference design from $D = 256$ until it reaches $\geq 99\%$ accuracy and the same number of iterations to converge compared to the proposed in-memory factorizer. We find that the dimension that achieves this behavior in the reference design is $D = 352$. This intermediate comparison point also lacks fairness because of the imbalance in the number of MAC operations consumed between the reference design and the proposed design.

Therefore we consider the final comparison point that involves larger dimensions and problem sizes. This is motivated by two factors.

1. With an increasing number of the dimensions, the reference design with deterministic behavior tends to achieve higher accuracies and a lower average number of iterations, even when the problem size is increased at the same rate. This allows comparison of hardware built with the same parameters which achieve the same algorithmic performance.
2. We have observed that the PCM crossbar array sizes can be scaled up to 512x512 size without compromising the noise levels. Furthermore, the energy of the analog core comprising the crossbar array is dominated by the analog peripherals whose energy scales linearly with the size of the crossbar. However, the energy scales quadratically in the reference design which relies on the digital processors.

We choose $D = 512$ and $M = 512$ as the parameter combination for the final comparison point. Our simulations find that under these parameter combinations the reference design and the proposed design achieve 100% accuracy with 6554 iterations and 6185 iterations on average respectively to factorize a query. The proposed design consumes 5.11 nJ to complete a single iteration, with

a breakdown of 2.09 nJ, 2.49 nJ, and 0.5 nJ shares for projection, similarity calculation, and the rest of the peripheral operations respectively.

The reference design with the parameters $D = 512$, $M = 256$ was found to be consuming 61.4 nJ energy to complete a single iteration. This can be split as 46.3 nJ, 14.5 nJ, and 0.5 nJ shares for the above-mentioned operational stages.

Table S3 summarizes all results. The total energy consumption for a single iteration as well as the average energy consumption for processing a single query until its factorization is complete in both designs are listed in the table. It can be seen that our proposed design outperforms the reference design by a factor of 13.1 \times , 13.9 \times and 4.85 \times when iteration energy, average query factorizing energy, and area savings are considered respectively in the final comparison point thanks to higher energy efficiency obtained when scaling up MVM operation using in-memory computing approach.

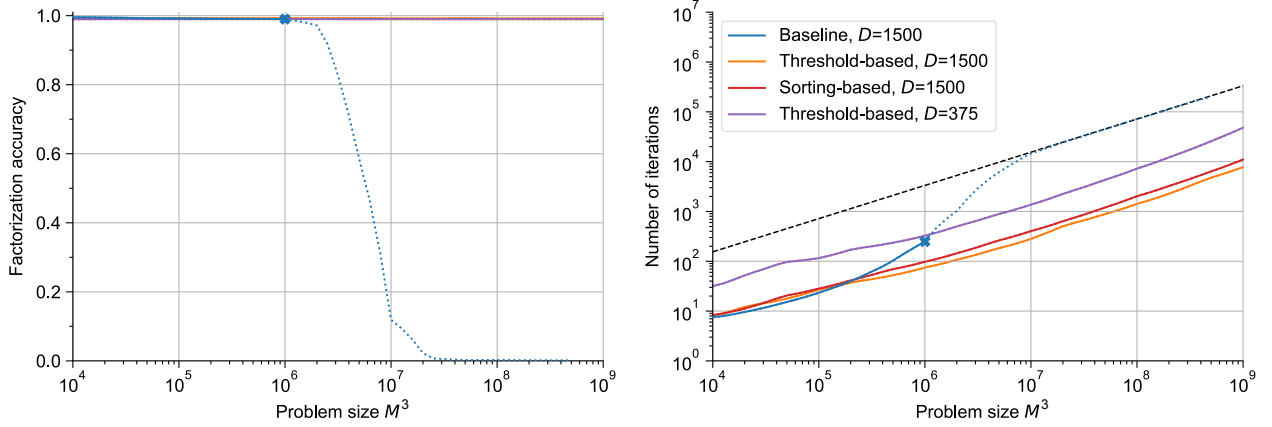


Fig. S1 | Comparison of the sorting-based and the threshold-based activations as well as lowering dimensionality. The first line visualizes the threshold-based activation for $F = 3$ at $D = 1500$. The second line shows the sorting-based activation at the place of the threshold-based activation. The last line shows the threshold-based activation for a lower dimension $D = 375$. The left side of the panel shows the accuracy for a wide range of problem sizes. It is clearly visible that the three aforementioned configurations reach an accuracy of 99% and higher. The right subpanel shows the average number of the iterations required to factorize a product vector for a wide range of the problem sizes. The threshold-based and the sorting-based activations perform equally at the same dimensionality of $D = 1500$. Lowering the dimensionality by roughly four times requires more iterations to factorize the same product, resulting in a trade of between dimensionality and time complexity. Compared to the baseline resonator, an in-memory factorizer with four times less dimensions is still capable of increasing the operational capacity.

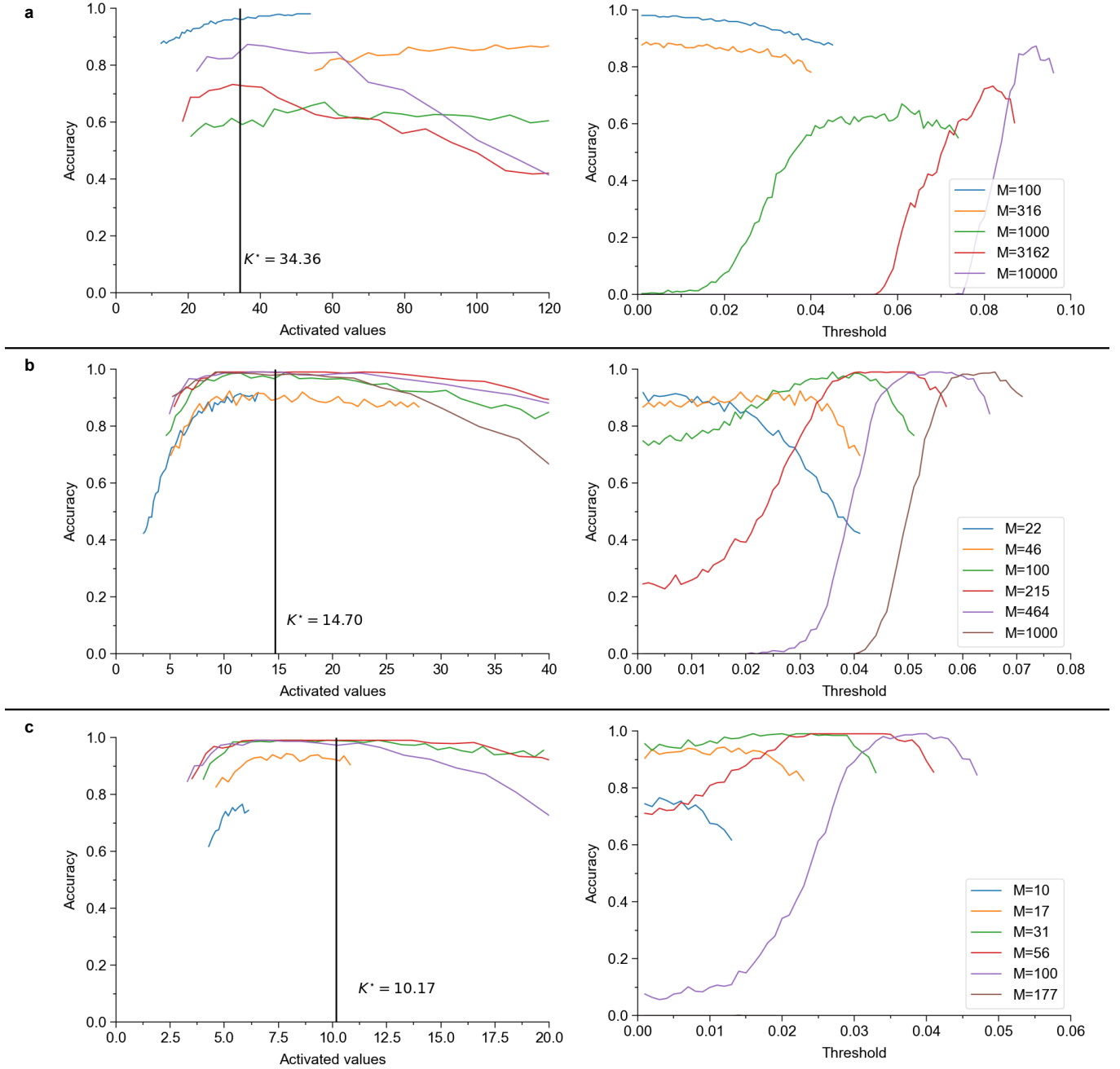


Fig. S2 | Mapping of the optimal number of the top K -activated values (K^*) to the corresponding threshold (T^*). The left half of this figure shows the optimal number of the top K -activated values: (a) for $F = 2$ and $D = 1000$; (b) for $F = 3$ and $D = 1500$; and (c) for $F = 4$ and $D = 2000$. The X-axis shows the number of the top K -activated values, and the Y-axis shows the accuracy of factorization. We limited the number of the iterations to $N' = 0.1 \times N$ to enforce the better solutions. Each line corresponds to a different codebook size such that the total problem size M^F ranges from $1e4$ to $1e9$. To get the curves displayed, we grid-searched the number of the activated values for each triplet D , F , and M . To convert the desired number of the activated values to a threshold we use the approach as in equations (S8) to (S12). The subpanels on the right side show the corresponding thresholds for the activated values curves. One can see that the best performing number of the top K -activated values is independent of M . The optimal number of the top K -activated values is averaged across all the optimas for each given codebook size.

TABLE S1 | Each given number of factors and dimension result in an optimal number of activated values.

| Factors (F) | 2 | | | | 3 | | | | 4 | | | |
|--------------------|-------|-------|-------|--------|------|-------|-------|-------|------|------|------|------|
| Dimensions (D) | 256 | 512 | 1024 | 2048 | 256 | 512 | 1024 | 2048 | 256 | 512 | 1024 | 2048 |
| Activated Values | 20.79 | 39.98 | 54.79 | 104.87 | 8.34 | 10.30 | 11.02 | 13.60 | 5.81 | 6.23 | 6.87 | 8.13 |

TABLE S2 | Operating conditions of the circuits.

| | Symbol | Value |
|-------------------------|------------|-------------------|
| Analog Circuits | | |
| Read Voltage | V_{read} | 0.1 V |
| Max Conductance | G_{max} | $10 \mu S$ |
| Source Line Capacitance | C_{SL} | 4 fF |
| Regulator Bias Current | I_{bias} | $50 \mu A$ |
| PWM circuit power | P_{FSM} | $54 \mu W$ |
| ADC conversion energy | E_{ADC} | 1.57 fJ/conv-step |
| Unit cell composition | - | 2T2R |
| Digital Circuits | | |
| Technology Node | - | 14 nm |
| Supply Voltage | VDD | 0.8 V |
| Operating Frequency | F | 10 MHz |
| Corner | - | Typical |
| Temperature | - | 25 °C |

TABLE S3 | Comparison between the proposed in-memory factorizer and an equivalent reference digital design.

| | | Reference | Proposed | Unit |
|--------------------------------------|-------|-----------|----------------------|------|
| Projection | | | | |
| Area | 4.6 | 0.551 | mm ² | |
| Time per Iteration | 100 | 40 | ns | |
| Energy per Iteration | 46.3 | 1.94 | nJ | |
| Peak Throughput | 5.24 | 13.1 | TOPS | |
| Energy Efficiency | 11.3 | 270 | TOPS/W | |
| Area Efficiency | 1.15 | 23.8 | TOPS/mm ² | |
| Similarity Calculation | | | | |
| Area | 0.865 | 0.551 | mm ² | |
| Time per Iteration | 100 | 10 | ns | |
| Energy per Iteration | 14.5 | 2.22 | nJ | |
| Peak Throughput | 5.24 | 52.4 | TOPS | |
| Energy Efficiency | 36.1 | 236 | TOPS/W | |
| Area Efficiency | 6.06 | 95.1 | TOPS/mm ² | |
| Other peripherals | | | | |
| Area | 24.3 | 24.3 | μm ² | |
| Time per Iteration | 300 | 300 | ns | |
| Energy per Iteration | 0.53 | 0.53 | nJ | |
| Totals | | | | |
| Area | 5.46 | 1.13 | mm ² | |
| Time per Iteration | 500 | 350 | ns | |
| Energy per Iteration | 61.4 | 4.70 | nJ | |
| Average Iterations per Factorization | 6553 | 6184 | - | |
| Time per Factorization | 3280 | 2164 | us | |
| Energy per Factorization | 402 | 29.0 | μJ | |